

Article

Robust Principal Component Thermography for Defect Detection in Composites

Samira Ebrahimi ¹, Julien Fleuret ¹, Matthieu Klein ², Louis-Daniel Th eroux ³, Marc Georges ⁴,
Clemente Ibarra-Castanedo ^{1,2,*} and Xavier Maldague ¹ 

¹ Computer Vision and Systems Laboratory (CVSL), Department of Electrical and Computer Engineering, Laval University, Quebec City, QC G1V 0A6, Canada; samira.ebrahimi.1@ulaval.ca (S.E.); julien.fleuret.1@ulaval.ca (J.F.); Xavier.Maldague@gel.ulaval.ca (X.M.)

² Infrared Thermography Testing Systems, Visioimage Inc., Quebec City, QC G1W 1A8, Canada; matthieu.klein@visioimage.com

³ Centre Technologique et A erospatial (CTA), Saint-Hubert, QC J3Y 8Y9, Canada; louis-daniel.theroux@cegepmontpetit.ca

⁴ Centre Spatial de Li ege, STAR Research Unit, Li ege Universit e, 4031 Angleur, Belgium; mgeorges@uliege.be

* Correspondence: ibarrac@gel.ulaval.ca



Citation: Ebrahimi, S.; Fleuret, J.; Klein, M.; Th eroux, L.; Georges, M.; Ibarra-Castanedo, C.; Maldague, X. Robust Principal Component Thermography for Defect Detection in Composites. *Sensors* **2021**, *21*, 2682. <https://doi.org/10.3390/s21082682>

Academic Editors: Vittorio M. N. Passaro, Leonhard Reindl, Assefa M. Melesse, Alexander Star, Eduard Llobet, Guillermo Villanueva and Mehmet Rasit Yuce

Received: 19 February 2021

Accepted: 7 April 2021

Published: 10 April 2021

Publisher's Note: MDPI stays neutral with regard to jurisdictional claims in published maps and institutional affiliations.



Copyright:   2021 by the authors. Licensee MDPI, Basel, Switzerland. This article is an open access article distributed under the terms and conditions of the Creative Commons Attribution (CC BY) license (<https://creativecommons.org/licenses/by/4.0/>).

Abstract: Pulsed Thermography (PT) data are usually affected by noise and as such most of the research effort in the last few years has been directed towards the development of advanced signal processing methods to improve defect detection. Among the numerous techniques that have been proposed, principal component thermography (PCT)—based on principal component analysis (PCA)—is one of the most effective in terms of defect contrast enhancement and data compression. However, it is well-known that PCA can be significantly affected in the presence of corrupted data (e.g., noise and outliers). Robust PCA (RPCA) has been recently proposed as an alternative statistical method that handles noisy data more properly by decomposing the input data into a low-rank matrix and a sparse matrix. We propose to process PT data by RPCA instead of PCA in order to improve defect detectability. The performance of the resulting approach, Robust Principal Component Thermography (RPCT)—based on RPCA, was evaluated with respect to PCT—based on PCA, using a CFRP sample containing artificially produced defects. We compared results quantitatively based on two metrics, Contrast-to-Noise Ratio (CNR), for defect detection capabilities, and the Jaccard similarity coefficient, for defect segmentation potential. CNR results were on average 40% higher for RPCT than for PCT, and the Jaccard index was slightly higher for RPCT (0.7395) than for PCT (0.7010). In terms of computational time, however, PCT was 11.5 times faster than RPCT. Further investigations are needed to assess RPCT performance on a wider range of materials and to optimize computational time.

Keywords: Robust PCA; RPCA; PCP; OIALM; Orthogonal IALM; noise reduction; pulsed thermography; CFRP

1. Introduction

The unique features that make carbon fiber reinforced plastics (CFRP) preferable to other materials are their high strength-to-weight ratio, good corrosion resistance, high fatigue resistance, and very low coefficient of thermal expansion. These interesting characteristics made CFRP a preferred choice in aerospace and other industries where manufacturing quality, weight, and user safety are of paramount importance. Non-destructive testing (NDT) techniques are regularly used to evaluate the efficiency and locate anomalies non-invasively. Infrared thermography (IRT) is a fast, non-contact, and non-invasive NDT approach to detect and characterize anomalies (surface or sub-surface defects) in materials. Pulsed thermography (PT) is one of the most popular active IRT approaches [1]. It is based on thermal heat transfer analysis in transient mode (during cooling).

In PT, a short pulse of energy is applied to the surface of the object being inspected; once the light reaches the sample, it becomes a thermal wave propagating through the material by conduction. An infrared camera records the surface temperature decay. Following the thermal pulse, materials without defects cool down uniformly. However, the presence of a discontinuity will change the diffusion rate, which will affect the heat distribution of the object. These thermal changes will appear at the surface at different times, depending on the properties of the object and the defects, as well as their depths. The deeper is the discontinuity, the later it is observed and the lower is its thermal contrast. However, pulsed thermography data is affected by electronic noise as well as thermal and optical artifacts that may reduce defect detectability. To extract meaningful information from the noisy recorded data, different mathematical methods have been proposed.

Principal component thermography (PCT) [2] is one of such processing methods, which is based on principal component analysis [3]. PCA is a tool for high-dimensional data processing that highlights the similarities and dissimilarities in data and estimates the low-dimensional subspace. As shown in [4], PCA can provide contrast enhancement and flaw depth estimation with a reconstructed data matrix. The goal of this method is to efficiently and accurately estimate the low intrinsic matrix lying on original data. Suppose matrix \mathbf{M} is a stacked column-vector of data:

$$\mathbf{M} = \mathbf{L} + \mathbf{S} \quad (1)$$

where \mathbf{L} has a low-rank and \mathbf{S} is a small perturbation matrix. Classical PCA looks for the rank- k estimate of \mathbf{L} by solving Equation (2):

$$\begin{aligned} & \text{Minimize } \|\mathbf{M} - \mathbf{L}\| \\ & \text{subject to : } \text{rank}(\mathbf{L}) \leq K \end{aligned} \quad (2)$$

where $\|\mathbf{M}\|$ denotes the 2-norm and $K \ll \min(m, n)$ is the target dimension of the subspace. In addition, when \mathbf{S} is small and independent and identically distributed (i.i.d) Gaussian noise, it is convenient to solve the problem via singular value decomposition (SVD). PCA works efficiently when the data enjoy a low level of noise; otherwise, in highly corrupted data, the estimated \mathbf{L} can be significantly affected.

Candès et al. [5] proposed an interesting method for rendering PCA more robust, where the objective is to recover the low-rank matrix \mathbf{L} from highly corrupted measurements \mathbf{M} . According to Candès et al., unlike classical PCA in which noise should be small, the entries in \mathbf{S} can have an arbitrarily large magnitude; therefore, it has been used on data containing high levels of noise, outliers, and distortions. To do so, Candès et al. decomposed the input data into a low-rank matrix and a sparse matrix, where the sparse matrix is an estimation of the noise in the data, and the low-rank matrix is an estimation of the data without noise. Candès et al.'s method is known as Robust Principal Component Analysis (RPCA).

RPCA has been used in a wide range of applications such as background estimation and foreground estimation [6], video surveillance [7], face recognition [8], speech recognition [9], latent segmentation indexing [10], and ranking and collaborative filtering to cite a few. Recently, Song et al. [11] employed the RPCA technique for noise reduction and signal enhancement in distributed detection of micro-cracks on structural elements with very small crack opening displacements. The method used by Candès et al. to decompose the data is known as principal component pursuit (PCP). Several other approaches in order to decompose input data into a low-rank matrix and sparse matrix have been proposed [7,12–14]. The minimization method used in the PCP has itself been the topic of many studies. Xue et al. [15] and Yang et al. [16] offered two new implementations of the PCP decomposition approach, named Exact Augmented Lagrange Multiplier (EALM) and Inexact Augmented Lagrange Multiplier (IALM). Guyon et al. [14] proposed to solve PCP by using a Linearized Alternating Direction Method with Adaptive Penalty (LADMAP), while Wang et al. studied the accelerated proximal gradient (APG) algorithm to solve it [7].

In this paper, we introduce a new variation for the decomposition by PCP. Then, we compare its performance with respect to the state-of-the-art PT processing techniques.

The paper is organized as follows. Section 2 introduces some recent works regarding both PT data processing as well as NDT applications using RPCA. In Section 3, we present the details of the proposed algorithm. Section 4 details the different aspects of our investigations. Section 5 introduces the results we obtained, while Section 6 analyzes and discusses the results we obtained. Finally, Section 7 concludes this study.

2. Literature Review

As previously stated, PT is a field that is eagerly searching for new processing methods to improve the detection of defects. Thus, over the years, several approaches have been proposed. In this section, we briefly introduce methods among the recently proposed.

Khan et al. [17] used a convolutional-auto-encoder-based approach for Intrusion detection, which is fast, simple, and efficient in terms of power and cybersecurity. In addition, Zhang et al. [18] developed an approach combining domain adaptation (DA) and adaptive convolutional neural network (ACNN) for steel surface defect detection, which showed an improved accuracy with respect to other methods.

Fleuret et al. [19] investigated the possible application of the Monogenic-Signal to PT data. Promising results were found; nevertheless, the method proved to be highly sensitive to noise. The same year, Yousefi et al. [20] studied an application of Sparse-PCA to PT, under the name SPCT, which outperformed existing methods in terms of defect detection although requiring a significantly higher computational time.

Wen et al. [21,22] used an improved version of the Sparse-PCA to speed up processing. This method named Edge-Group Sparse PCA (ESPCT) [23] was significantly faster than SPCT, although still noticeably slower than PCT. It offered higher defect contrast, making it very promising for the detection of smaller defects in composite materials.

Yousefi et al. [20,24,25] investigated the application of several non-negative matrix factorization (NMF) methods on a wide set of materials. These studies highlighted that NMF offers noticeably better results than other component-based approaches.

The implementation of independent component analysis (ICA) on pulsed thermography inspection of CFRP has been investigated by several authors [26–28]. Rengifo et al. [26] reported achieving a sensitivity of 70% on a sample test. Liu et al. [27] highlighted the ability of the ICA to handle thermal inhomogeneities, and other noise sources, as well as providing good defect contrast. Fleuret et al. [28] observed that ICA was comparable to PCT in terms of performance, but with the advantage of being less sensitive to background noise.

Fleuret et al. [29] investigated the application of another approach named Latent Low-Rank Representation (LatLRR) to PT data under the name LatLRRT. This approach differs from most of the previous works because it is based on the assumption that the data are composed of three signals: the observed data, the sparse noise, and the unobserved data. The authors concluded that LatLRRT used as a post-processing method can significantly improve results with respect to state-of-the-art approaches such as PPT [30]. Nevertheless, for the moment, the memory cost prevents this method from being used as a processing method.

Recently, Liu et al. [31] introduced an approach that uses data augmentation generated by the deep-learning models. The assumption was that deep-learning models would be able to learn statistical features from the data. Liu et al.'s method provided good results on composite materials compared with state-of-the-art methods such as PCT [4,32]. The same authors evaluated their work using ICA as a detection method [33]. Similar to the previous one, this method provides good results on composite materials.

Lopez et al. [34,35] proposed partial least square (PLS) regression to improve the general quality of the image sequences. During the regression step, the PLS algorithm can model both spatially and temporally the evolution of the signal. It was originally proposed as a denoising technique allowing synthetic data reconstruction in a manner similar to thermographic signal reconstruction (TSR) [36].

Inspired by these works, Fleuret et al. [37] investigated the use of a pair of support vector machine (SVM) algorithms [38] to enhance defect contrast. The first algorithm computes a regression in the time domain, while the second computes a regression in the space domain. Then, the output sequence is reconstructed from these regressions providing images with enhanced defect contrast.

Even though RPCA is a well-known tool for background-foreground subtraction with improved robustness to noise in several imaging application, it has seldom been investigated in infrared thermography. Zhu et al. [39,40] used RPCA to reduce noise from eddy current pulsed thermography (ECPT) data. Their work was based on the RPCA method proposed by Candès et al. [5]. Liang et al. [41] studied the use of a tensor-based RPCA approach proposed by Lu et al. [42] on ECPT. They concluded that TRPCA is a high accuracy defect extraction algorithm. Xiao et al. [43] studied the application of yet another type of RPCA for data fusion.

The RPCA method we proposed is inspired by the work of Candès et al. [5], however more recent works have been suggested since then. For instance, Peng et al. [44] proposed a highly scalable convex RPCA based on ALM and matrix factorization. Sun et al. [45] proposed a graph-based RPCA. Liu et al. [46] also proposed a graph-based method that has the advantage of being adaptive, ensuring in this way that the local structure of the data is well represented in the low-rank matrix.

Wang et al. [47] introduced the Double RPCA (DRPCA), which offers increased robustness regarding the topology of the regions in the image. In addition, unlike most of the RPCA approaches, which are transductive, DRPCA is an inductive approach, which makes it suitable for online application. Ma et al. [48] offered a review of the most popular RPCA methods used for convex optimization. Van Luong et al. [49] proposed an RPCA method for online application such as background and foreground separation. Cai et al. [50] introduced a rapid RPCA based on an accelerated inexact low-rank estimation.

Several other methods can be found in the literature. We included here a selection of studies on which we based our approach. In particular, our choice regarding the work of Candès et al. [5] is due to the stability and robustness of their approach, which for these reasons has become a reference. Nonetheless, as detailed in next section, our proposed approach is better adapted for the PT applications.

3. RPCA via OIALM

Among the different methods proposed in the literature to overcome the limitation of the PCA regarding noisy data, the one proposed by Candès et al. [5] has become very popular. In their work, Candès et al. used a convex optimization; the formulation they used is known as principal component pursuit (PCP). Other formulations and improvements of the PCP, have since been proposed. In particular, the work of Lin et al. [51] has become well-known due to its ability to converge faster than similar methods such as accelerated proximal gradient (APG).

Lin et al. proposed two variations of the PCP formulation using the augmented Lagrangian multiplier (ALM) approach, named Exact Augmented Lagrangian Multiplier (EALM) method and Inexact Augmented Lagrangian Multiplier (IALM). Even though both methods attempt to optimize the sparse and low-rank matrix, their main difference is a condition applied on a set of penalty parameters that allow the IALM algorithm to converge faster than EALM by avoiding the minimization of a sub-problem.

Our approach is inspired by the IALM formulation. Given an observation matrix \mathbf{D} , which is assumed to be the combination of two matrices, \mathbf{A} (low-rank) and \mathbf{E} (a sparse matrix), the straightforward formulation to minimize the energy function is to use the l_0 -norm:

$$\begin{aligned} \min \text{rank}(\mathbf{A}) + \lambda \|\mathbf{E}\|_0 \\ \mathbf{D} = \mathbf{A} + \mathbf{E} \end{aligned} \quad (3)$$

where $\|\cdot\|_0$ is the l_0 -norm, that is, the number of the non-zero items of the matrix, and implies the sparsity. λ is the balance parameter to determine the contributions of \mathbf{A} and \mathbf{E} in minimizing the objective function. Since Equation (3) is an NP-hard problem, i.e., at least as hard as the hardest problems in non-deterministic polynomial (NP) time, Candès et al. [5] reformulated this equation into a similar convex optimization problem as follows:

$$\begin{aligned} \min_{\mathbf{L}, \mathbf{S}} (\|\mathbf{A}\|_* + \lambda \|\mathbf{E}\|_1) \\ \text{subject to } \mathbf{D} = \mathbf{A} + \mathbf{E} \end{aligned} \quad (4)$$

where $\|\mathbf{A}\|_*$ and $\|\mathbf{E}\|_1$ are the nuclear norm of \mathbf{A} and l_1 -norm of \mathbf{E} , respectively. The balance parameter λ is defined as:

$$\lambda = 1 / \sqrt{\max(m, n)} \quad (5)$$

where m is the number of rows and n is the number of columns of the 2D input matrix. Lin et al. [51] solved Equation (4) using a generic ALM method, which solves the constrained optimization problem:

$$\begin{aligned} \min f(x), \text{ subject to } h(x) = 0 \\ f : \mathbb{R}^n \rightarrow \mathbb{R}, h : \mathbb{R}^n \rightarrow \mathbb{R}^m \end{aligned} \quad (6)$$

The Lagrange function can be defined as:

$$L(\mathbf{X}, \mathbf{Y}, \mu) = f(\mathbf{X}) + \langle \mathbf{Y}, h(\mathbf{X}) \rangle + \frac{\mu}{2} \|h(\mathbf{X})\|_F^2 \quad (7)$$

According to the Lagrange multiplier method, Equation (6) can be reformulated to solve the RPCA problem as follows:

$$\begin{aligned} \mathbf{X} = (\mathbf{A}, \mathbf{E}), f(\mathbf{X}) = \|\mathbf{A}\|_* + \lambda \|\mathbf{E}\|_1. \\ h(\mathbf{X}) = \mathbf{D} - \mathbf{A} - \mathbf{E} \end{aligned} \quad (8)$$

The Lagrange function of Equation (8) is defined as:

$$L(\mathbf{A}, \mathbf{E}, \mathbf{Y}, \mu) = \|\mathbf{A}\|_* + \lambda \|\mathbf{E}\|_1 + \langle \mathbf{Y}, \mathbf{D} - \mathbf{A} - \mathbf{E} \rangle + \frac{\mu}{2} \|\mathbf{D} - \mathbf{A} - \mathbf{E}\|_F^2 \quad (9)$$

where \mathbf{Y} is the Lagrange multiplier and penalty parameter μ is a positive scalar parameter. The approximate exact augmented Lagrange multiplier algorithm used to solve the RPCA problem is shown in Algorithm 1. \mathbf{Y}_0 has been initialized to $\mathbf{Y}_0 = \mathbf{D} / J(\mathbf{D})$ [52], making the objective function value $\langle \mathbf{Y}_0, \mathbf{D} \rangle$ reasonably large. In addition, $J(\mathbf{D}) = \max(\|\mathbf{A}\|_2, \lambda^{-1} \|\mathbf{Y}\|_\infty)$, where $\|\cdot\|_\infty$ is the maximum absolute value of the input matrix. In each iteration after solving \mathbf{A}_{k+1} and \mathbf{E}_{k+1} , the low-rank matrix \mathbf{L} is updated by Incremental-PCA [53].

In Step 1 of Algorithm 1, ρ is the learning rate and μ_0 is the initialization of the penalty parameter that influences the convergence speed. In [51], it is proven that the objective function of the RPCA problem (Equation (4)), which is non-smooth, has an excellent convergence property. In addition, it has been proven that, to converge to an optimal solution $(\mathbf{A}^*, \mathbf{E}^*)$ of the RPCA problem, it is necessary for μ_k to be non-decreasing and $\sum_{k=1}^{+\infty} \mu_k^{-1} = +\infty$. As can be noticed from Equation (10), our proposed approach differs

from the IALM in that the low-rank matrix is projected into an orthogonal space, which is why we named this approach Orthogonal IALM:

$$\begin{aligned}\mathbf{A}_{k+1} &= \underset{\mathbf{u} \in \mathbb{R}^n}{\operatorname{argmax}} \mathbf{u}^T \mathbf{A}_{k+1}^T \mathbf{A}_{k+1} \mathbf{u} \\ &= \underset{\mathbf{u} \in \mathbb{R}^n}{\operatorname{argmax}} \mathbf{u}^T \mathbf{C} \mathbf{u}\end{aligned}\quad (10)$$

where \mathbf{u} is a unit vector so $\mathbf{u}^T \mathbf{u} = 1$. This projects the low-rank value into an orthogonal space while maximizing the variance between the projected data. This step provides relevant information to be projected among the projected matrix's first dimensions; therefore, it is possible to reduce the computational cost by only keeping γ dimensions, which corresponds to a PCA.

Algorithm 1: RPCA via the Orthogonal IALM method

Input: Data: $\mathbf{D} \in \mathbb{R}^{m \times n}$, balance parameter λ , dimensionality reduction scalar: $\gamma (\leq n)$
 $\mathbf{Y}_0 = \frac{\mathbf{D}}{J(\mathbf{D})}; E_0 = 0; \mu_0 > 0; \rho > 1; k = 0;$
while not converged do
 // Lines 3-4 update A by solving $\mathbf{A}_{k+1} = \underset{\mathbf{A}}{\operatorname{argmin}} L(\mathbf{A}, \mathbf{E}_k, \mathbf{Y}_k, \mu_k)$
 $(\mathbf{U}, \mathbf{S}, \mathbf{V}) = \operatorname{svd}(\mathbf{D} - \mathbf{E}_k + \mu_k^{-1} \mathbf{Y}_k);$
 $\mathbf{A}_{k+1} = \mathbf{U} \mathbf{S}_{\mu_k^{-1}} [\mathbf{S}] \mathbf{V}^T;$
 // Line 5 update E by solving $\mathbf{E}_{k+1} = \underset{\mathbf{E}}{\operatorname{argmin}} L(\mathbf{A}_{k+1}, \mathbf{E}, \mathbf{Y}_k, \mu_k)$
 $\mathbf{E}_{k+1} = \mathcal{S}_{\lambda \mu_k^{-1}} [\mathbf{D} - \mathbf{A}_{k+1} + \mu_k^{-1} \mathbf{Y}_k];$
 // Lines 6 Updating A by solving $\mathbf{A}_{k+1} = \underset{\mathbf{u} \in \mathbb{R}^n}{\operatorname{argmax}} \mathbf{u}^T \mathbf{A}_{k+1}^T \mathbf{A}_{k+1} \mathbf{u}$
 $\mathbf{A}_{k+1} = \underset{\mathbf{u} \in \mathbb{R}^n}{\operatorname{argmax}} \mathbf{u}^T \mathbf{A}_{k+1}^T \mathbf{A}_{k+1} \mathbf{u};$
 $\mathbf{Y}_{k+1} = \mathbf{Y}_k + \mu_k (\mathbf{D} - \mathbf{A}_{k+1} - \mathbf{E}_{k+1});$
 $\mathbf{Y}_{k+1} = \{\mathbf{Y}_{k+1}^1, \mathbf{Y}_{k+1}^2, \dots, \mathbf{Y}_{k+1}^\gamma\};$
 Update μ_k to $\mu_{k+1};$
 $k \leftarrow k + 1;$
end
Output: $(\mathbf{A}_k, \mathbf{E}_k)$

In the next section, we describe our experiments and analysis and present our data.

4. Methods

In the previous section, we introduce RPCA. Now, we describe the different aspects of the experiments we conducted in order to evaluate its performance. Figure 1a shows our research block diagram, which presents all of the steps.

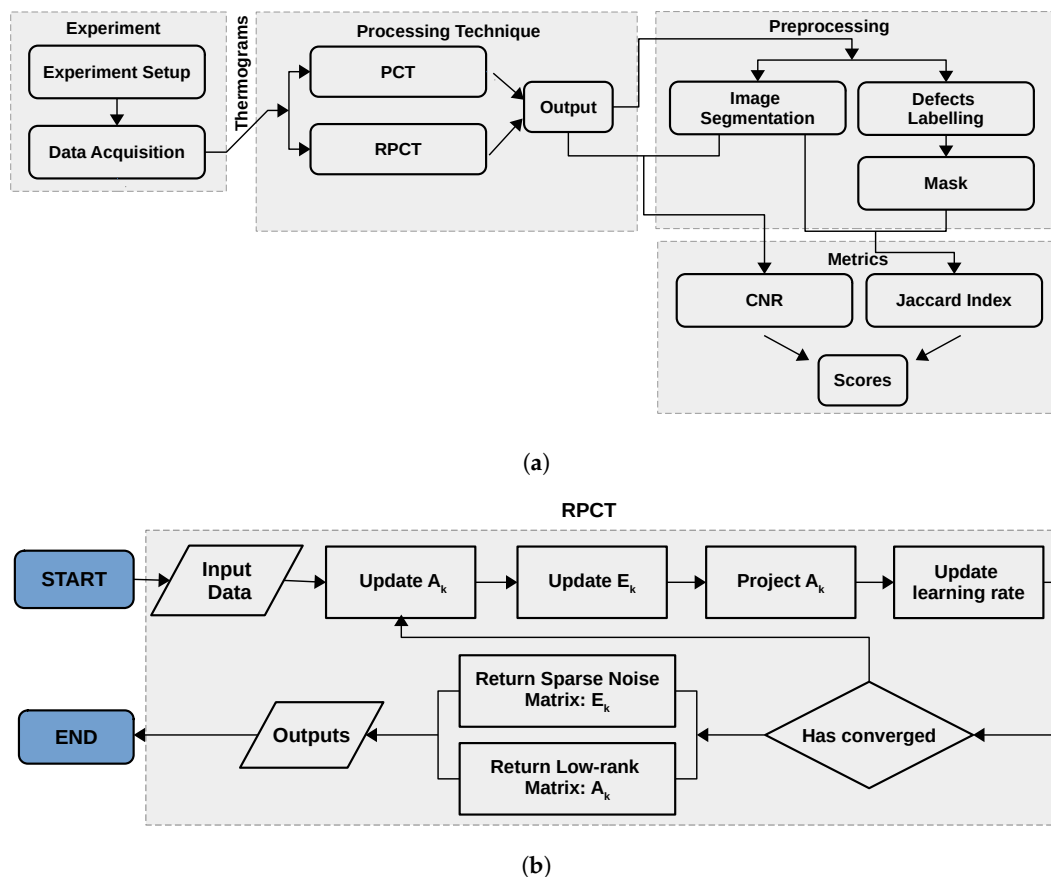


Figure 1. (a) Research block diagram; and (b) proposed method block diagram.

4.1. Data Acquisition

An academic CFRP plate (30.8 cm × 46 cm × 2.57 mm) was used in this study. It possesses 73 defects of three different types: 23 round flat-bottom holes (FBH), 25 triangular Teflon inserts, and 25 triangular pullouts. These types of manufactured flaws are employed to represent delaminations in CFRP laminates in Ultrasonic Testing because the change in acoustic impedance between the composite and the defect (Teflon or air) produces a variation in the ultrasonic signal when it passes through [54]. This plate was already used to study the adequateness of such artificial defects to represent delamination in thermography and shearography NDT [55] as well as for research on PCA analysis in shearography [56,57]. Defect size, depth, and thickness are indicated in Table 1, and their respective locations are shown in Figure 2a.

The PT experimental setup consists of two flash lamps (5 ms thermal pulse, 6.4 KJ/flash (Balcar, France)), a cooled infrared camera (FLIR Phoenix (FLIR Systems, Inc., Wilsonville, OR, USA), InSb, midwave, 3–5 mm, Stirling Cooling), and a computer to store the thermal sequences. The data were acquired at a frequency of 180 Hz. A control unit was also required to control and synchronize the data acquisition with flash triggering. Our experiments were performed using a PC (Intel(R) Xeon(R), 128 Gb memory, (Intel Corporation, Santa Clara, CA, USA)). Figure 2b, shows the PT approach in reflection mode.

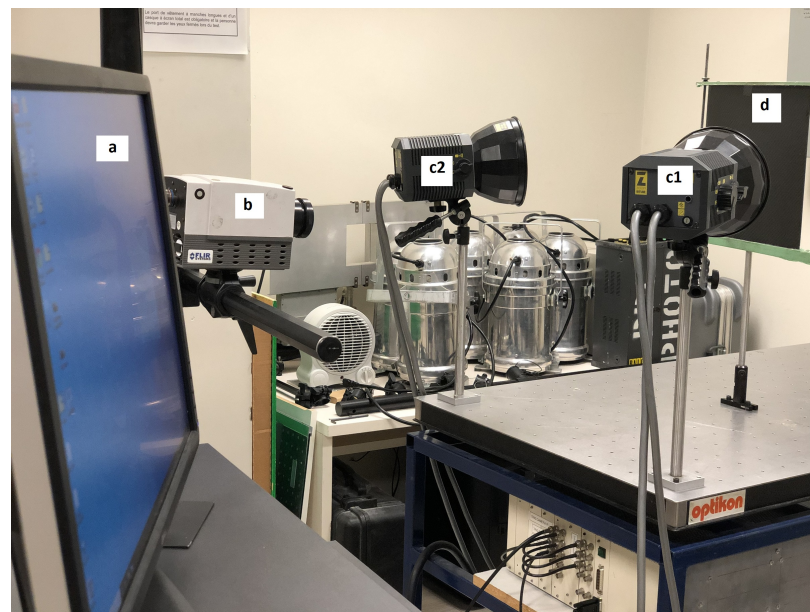
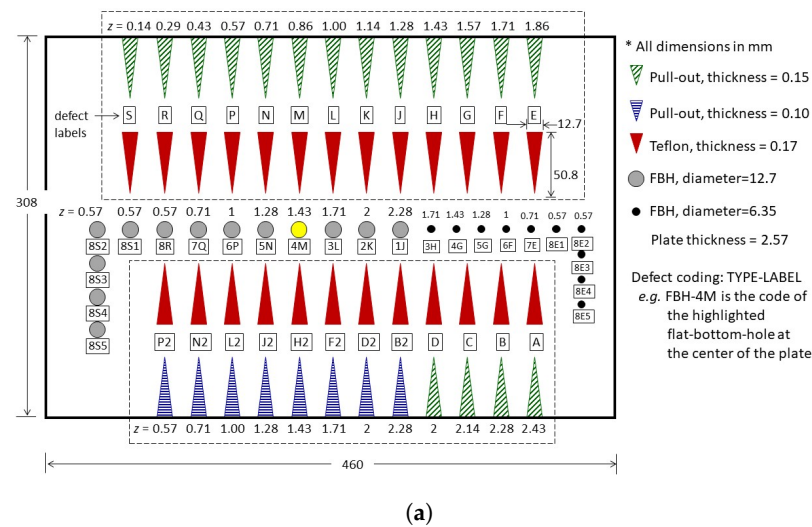


Figure 2. (a) CTA CFRP plate, where Z is the defect depth and labels are used to identify the location of each defect; and (b) pulsed thermography setup. a, PC; b, IR camera; c1 and c2, left and right flashes; d, CFRP specimen.

4.2. Metrics

In this section, we briefly introduce the different metrics we used to quantitatively assess the performance of our proposed approach RPCT, and compare it to PCT.

4.2.1. Contrast to Noise Ratio (CNR)

The Signal-to-noise ratio (SNR) is a metric that measures image quality by estimating the signal level with respect to the background noise. The Contrast-to-noise ratio (CNR) is similar to SNR although based on the difference (i.e., the contrast) between two features in an image. This contrast can be calculated, for instance, for a defect area with respect to a sound area. This is interesting since it provides a tool to quantitatively assess the defect detection capabilities of a given method. Several CNR definitions can be found in the literature, as summarized by Usamentiaga et al. [58]. This study also proposes to use the following definition, as it has been shown to be the most robust against noise and image enhancement operations (e.g., Gamma correction):

$$CNR = \frac{|\mu_S - \mu_N|}{\sqrt{\frac{(\sigma_S^2 + \sigma_N^2)}{2}}} \quad (11)$$

where μ_S is average level of the signal in the defect region, μ_N is the average level of the noise in the sound area, σ_S is standard deviation of the signal in the defect area, and σ_N is standard deviation of the noise in the reference region.

Table 1. Defect specifications for the CFRP Plate, Z is the depth of the defect below the inspected surface. Thickness is the defect thickness or thickness of the holes in case of the FBH type of defect.

Defect Code	Z [mm]	Dimensions [mm]	Thickness [mm]	Defect Code	Z [mm]	Dimensions [mm]	Thickness [mm]	Defect Code	Z [mm]	Dimensions [mm]	Thickness [mm]
Teflon Inserts				Pull-Outs				FlatBottom Holes			
Tef-A	2.43	12.7 × 50.8	0.17	PO15-A	2.43	12.7 × 50.8	0.15	FBH-1J	2.28	12.70	0.29
Tef-B	2.28	12.7 × 50.8	0.17	PO15-B	2.28	12.7 × 50.8	0.15	FBH-2K	2.00	12.70	0.57
Tef-C	2.14	12.7 × 50.8	0.17	PO15-C	2.14	12.7 × 50.8	0.15	FBH-3L	1.71	12.70	0.86
Tef-D	2.00	12.7 × 50.8	0.17	PO15-D	2.00	12.7 × 50.8	0.15	FBH-4M	1.43	12.70	1.14
Tef-E	1.86	12.7 × 50.8	0.17	PO15-E	1.86	12.7 × 50.8	0.15	FBH-5N	1.28	12.70	1.29
Tef-F	1.71	12.7 × 50.8	0.17	PO15-F	1.71	12.7 × 50.8	0.15	FBH-6P	1.00	12.70	1.57
Tef-G	1.57	12.7 × 50.8	0.17	PO15-G	1.57	12.7 × 50.8	0.15	FBH-7Q	0.71	12.70	1.86
Tef-H	1.43	12.7 × 50.8	0.17	PO15-H	1.43	12.7 × 50.8	0.15	FBH-8R	0.57	12.70	2.00
Tef-J	1.28	12.7 × 50.8	0.17	PO15-J	1.28	12.7 × 50.8	0.15	FBH-8S1	0.57	12.70	2.00
Tef-K	1.14	12.7 × 50.8	0.17	PO15-K	1.14	12.7 × 50.8	0.15	FBH-8S2	0.57	12.70	2.00
Tef-L	1.00	12.7 × 50.8	0.17	PO15-L	1.00	12.7 × 50.8	0.15	FBH-8S3	0.57	12.70	2.00
Tef-M	0.86	12.7 × 50.8	0.17	PO15-M	0.86	12.7 × 50.8	0.15	FBH-8S4	0.57	12.70	2.00
Tef-N	0.71	12.7 × 50.8	0.17	PO15-N	0.71	12.7 × 50.8	0.15	FBH-8S5	0.57	12.70	2.00
Tef-P	0.57	12.7 × 50.8	0.17	PO15-P	0.57	12.7 × 50.8	0.15	FBH-3H	1.71	6.35	0.86
Tef-Q	0.43	12.7 × 50.8	0.17	PO15-Q	0.43	12.7 × 50.8	0.15	FBH-4G	1.43	6.35	1.14
Tef-R	0.29	12.7 × 50.8	0.17	PO15-R	0.29	12.7 × 50.8	0.15	FBH-5G	1.28	6.35	1.29
Tef-S	0.14	12.7 × 50.8	0.17	PO15-S	0.14	12.7 × 50.8	0.15	FBH-6F	1.00	6.35	1.57
Tef-B2	2.28	12.7 × 50.8	0.17	PO10-B2	2.28	12.7 × 50.8	0.10	FBH-7E	0.71	6.35	1.86
Tef-D2	2.00	12.7 × 50.8	0.17	PO10-D2	2.00	12.7 × 50.8	0.10	FBH-8E1	0.57	6.35	2.00
Tef-F2	1.71	12.7 × 50.8	0.17	PO10-F2	1.71	12.7 × 50.8	0.10	FBH-8E2	0.57	6.35	2.00
Tef-H2	1.43	12.7 × 50.8	0.17	PO10-H2	1.43	12.7 × 50.8	0.10	FBH-8E3	0.57	6.35	2.00
Tef-J2	1.28	12.7 × 50.8	0.17	PO10-J2	1.28	12.7 × 50.8	0.10	FBH-8E4	0.57	6.35	2.00
Tef-L2	1.00	12.7 × 50.8	0.17	PO10-L2	1.00	12.7 × 50.8	0.10	FBH-8E5	0.57	6.35	2.00
Tef-N2	0.71	12.7 × 50.8	0.17	PO10-N2	0.71	12.7 × 50.8	0.10				
Tef-P2	0.57	12.7 × 50.8	0.17	PO10-P2	0.57	12.7 × 50.8	0.10				

4.2.2. Jaccard Similarity Coefficient Score

The Jaccard similarity coefficient (also known as Jaccard index or Intersection-Over-Union (IoU)), initially proposed by Paul Jaccard [59], is a statistical method that measures the similarity between two datasets and is defined as the ratio of the intersection size to the union size of two sample sets (as illustrated in Figure 3). The Jaccard index is a useful and very straightforward metric.

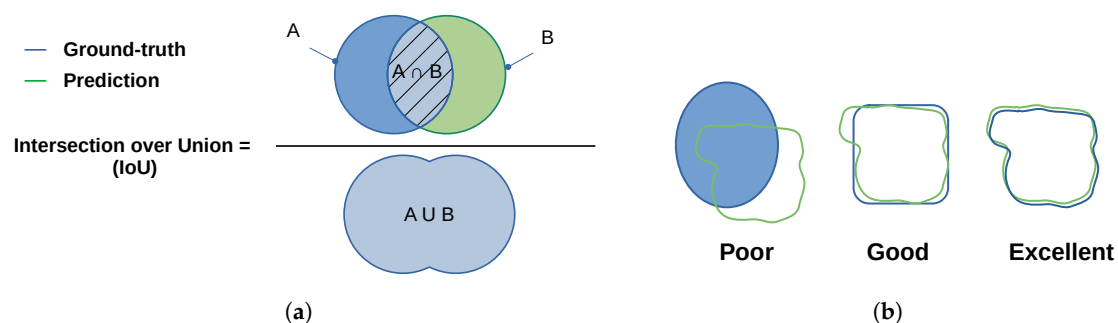


Figure 3. (a) Jaccard Index similarity definition; and (b) similarity between the ground-truth and the detected area.

In this approach, four steps should be taken into account:

1. Count the number of members (i.e., pixels) that are shared between both sets (intersection).
2. Count the total number of members in both sets i.e., the union (shared and unshared).
3. Divide the number of shared members (1) by the total number of members (2).
4. Multiply the computed result from Step 3 by 100.

$J(\mathbf{A}, \mathbf{B})$ provides a value between 0 (no similarity) and 1 (identical sets). Hence, the higher is the value of IoU, the higher is the level of similarities between two sets (Figure 3b).

$$J(\mathbf{A}, \mathbf{B}) = \frac{|\mathbf{A} \cap \mathbf{B}|}{|\mathbf{A} \cup \mathbf{B}|} = \frac{|\mathbf{A} \cap \mathbf{B}|}{|\mathbf{A}| + |\mathbf{B}| - |\mathbf{A} \cap \mathbf{B}|} \quad (12)$$

$$0 \leq J(\mathbf{A}, \mathbf{B}) \leq 1$$

4.3. Analysis

We chose to compare our approach RPCT that is based on RPCA, with principal component thermography (PCT) [32] that is based on PCA, to verify if the use of RPCA will effectively reduce the impact of noise.

The calculation of the score for each one of our two metrics was carried out using two different protocols. For the calculation of the Jaccard Index, we developed a custom automatic segmentation approach, as illustrated in Figure 4. This approach is based on four steps: First, the image's contrast is corrected using a percentile normalization between the second and ninety-eighth percentiles. The choice of the percentile normalization is due to the ability of this approach to increase the contrast even in the presence of local light artifacts. Then, a bilateral filter [60] is used to smooth the image. To smooth efficiently, we selected a spatial filter with a kernel of size 31×31 pixels and a range filter with kernel of size 7×7 pixels. The third step consists in applying a local thresholding approach based on a block of 101×101 pixels. The last step consists in removing the small objects in 2 connectivity with smaller than 64 pixels present in the image. The reason for the latter step is to remove artifacts that could have been generated by the third step.

Once the images of the different methods are segmented, they can be compared with a manually labeled reference image in order to compute the metric score.

Regarding the CNR score, before the experiments, both the defect regions and sound areas were manually labeled, as can be seen in the two examples shown in Figure 5, where three boundaries can be seen: red, green and blue. The sound area is located in between the outermost boundary (in red) and the middle boundary (in green), while the defect area corresponds to the area inside the innermost boundary (in blue). The average and standard deviation values required in Equation (11) are calculated from these areas. The exact same areas were used to estimate the CNR values from raw, PCT, and RPCT data.

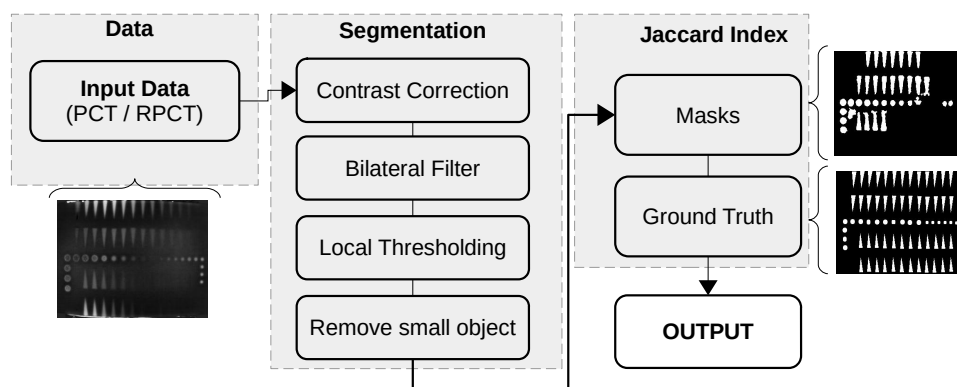


Figure 4. Segmentation and Jaccard index computation flow graph.

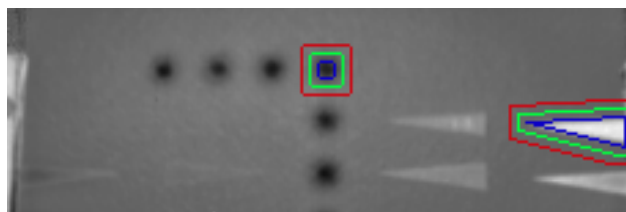


Figure 5. Examples of reference and defect regions. The boundaries of the reference region are between the green and red lines, while the defective region is inside the blue line area.

The following section presents the results.

5. Results

The original PT sequence (raw data) was processed by PCT and RPCT. Figure 6 shows some representative results (selected arbitrarily) of the different methods.

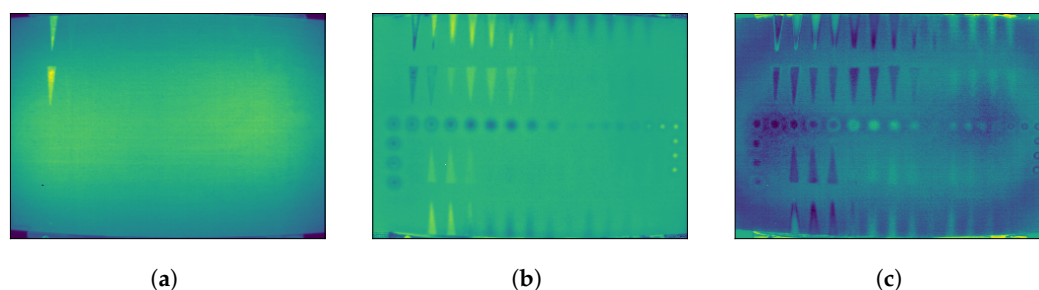


Figure 6. (a) Raw data at Frame 5; (b) fifth component of PCT data; and (c) fifth component of RPCT data.

Raw data correspond to the original unprocessed data. The arithmetical difference between a defective and a non-defective (sound) pixel (or group of pixels) is called the absolute thermal contrast, or simply the contrast. A given defect would be visible, i.e., its contrast would be higher than zero during a certain time that depends on different factors (defect type, size and depth, inspection method, amount of delivered energy, etc.). The thermal contrast typically varies from zero to a maximum, and then it gradually returns to zero. For instance, considering defect FBH-4M (at the center of the plate, highlighted in Figure 7), Figure 7 shows the thermal profiles, i.e., temperature vs. time plots, for a pixel inside the defect area (red plot), the profile of a pixel in the sound pixel close to this defect (blue plot), and the thermal contrast (green plot).

Hence, defects are visible at different degrees during several frames. In the case illustrated in Figure 7, defect FBH-4M can be detected roughly from 0.1 to 10 s, which corresponds to the time range where the contrast is higher than the noise. All other defects in the inspected plate produce similar profiles, with deeper defects appearing later and with lesser contrast.

PCT and RPCT, on the other hand, are statistical methods based on PCA and RPCA, respectively, that reorder data according to their variability and project them into an orthonormal space in such a way that the most valuable information is compressed in the first few components while subsequent components contain mostly noise. Figure 8 shows some selected PCT components: (Figure 8a) first PCT component showing several defects but also a strong non-uniform heating pattern (two ellipses, left and right) that accounts for most of the variability of the data and are therefore concentrated in the first component; (Figure 8b,c) second and third components, respectively, showing most of the defects and lesser impact from non-uniform heating; and (Figure 8d,f) later components (21st, 500th, and 3500th, respectively) showing mostly noise.

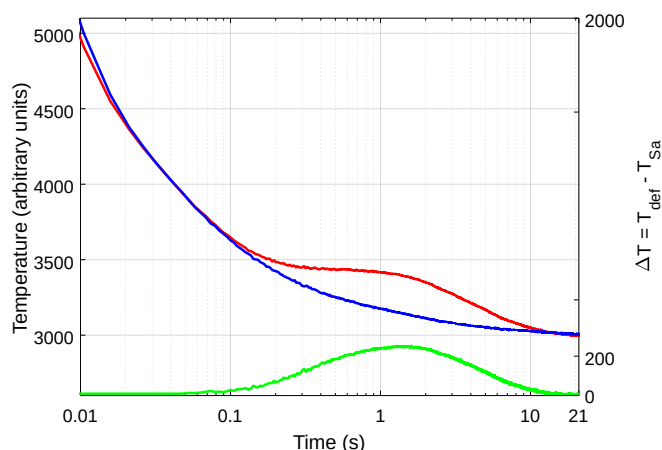


Figure 7. Thermal profiles (temperature vs. time plots on a semi-logarithmic scale) of a pixel inside defect FBH-4M (red plot); a sound pixel close to this defect (blue plot); and the absolute thermal contrast between these two (green plot).

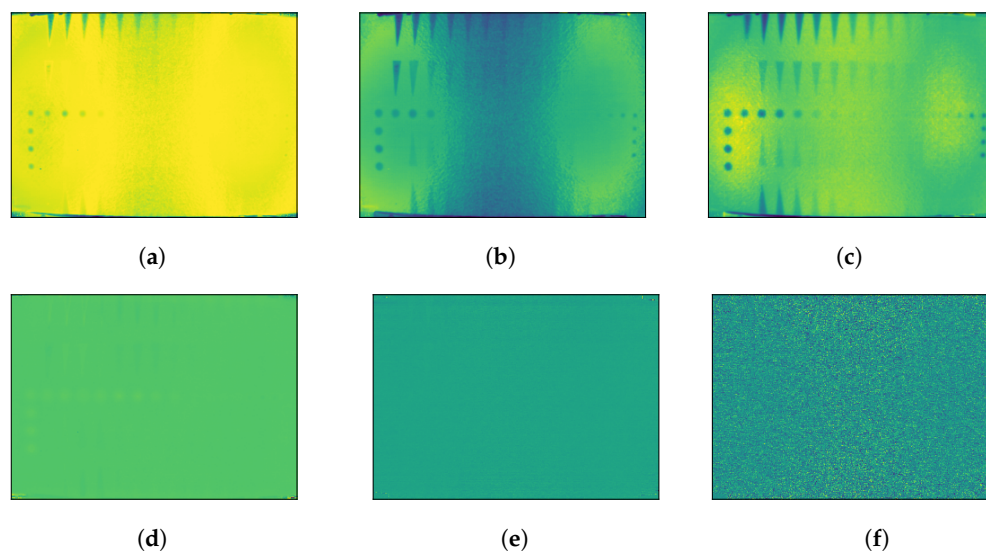


Figure 8. PCT components: (a) first; (b) second; (c) third; (d) 21st; (e) 500th; and (f) 3500th.

Table 2 summarizes the computational time for each of the processing techniques. As can be seen, RPCT takes significantly more time to compute (483 s) than PCT (42 s). Further optimization of the processing algorithm would be required to reduce this gap.

Table 2. Processing time of RPCT and PCT methods.

Process	RPCT	PCT
Run time (sec)	483.06	42.007
ROI size (px)	229 × 320	229 × 320
Number of frames	3998	3998

The CNR values of all defects and all processing techniques were calculated using the defects and reference areas as the ones shown in Figure 5. The highest CNR value (CNR_{max}) was then found for each case and the results are summarized in Table 3. The maximum CNR values between different methods are in bold.

Figure 9 presents selected CNR curves for raw, PCT, and RPCT data that correspond to defects at the same depth ($Z = 1.43$ mm) but of different types (FBH, pull-outs, and inserts) in which the CNR_{max} value is indicated together with the frame of occurrence.

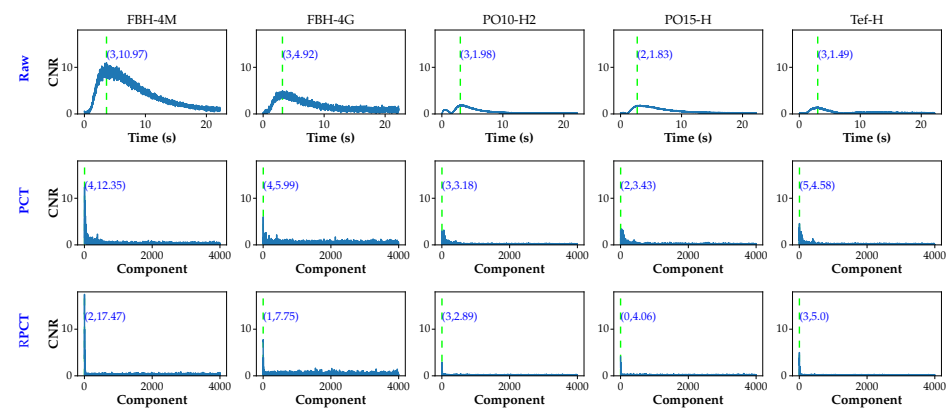


Figure 9. Comparative CNR curves for defects at the same depth ($Z=1.43$ mm) but different types (FBH, pull-outs and inserts): (**Row 1**) raw data; (**Row 2**) PCT; and (**Row 3**) RPCT. Columns 1–5 represent FBH-4M, FBH-4G, PO10-F2, PO15-H, and Tef-H, respectively.

To further analyze results, the CNRmax values are gathered by defect type in Figure 10 and by defect depth in Figure 11.

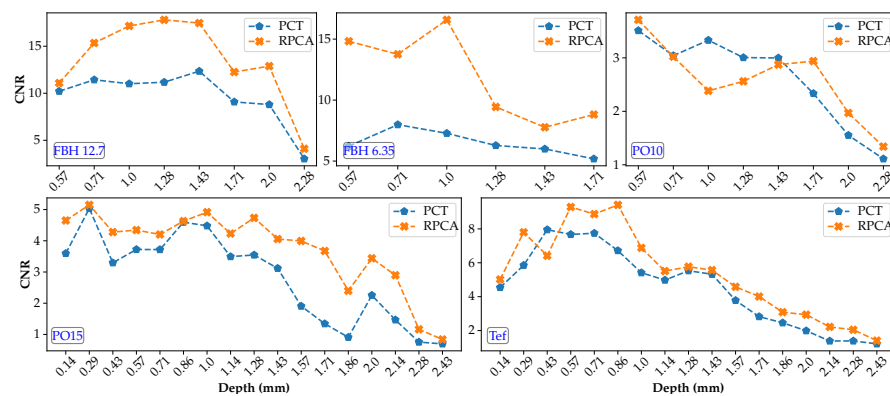


Figure 10. CNRmax by defect type as a function of the defect depth for all data sequences (PCT and RPCT).

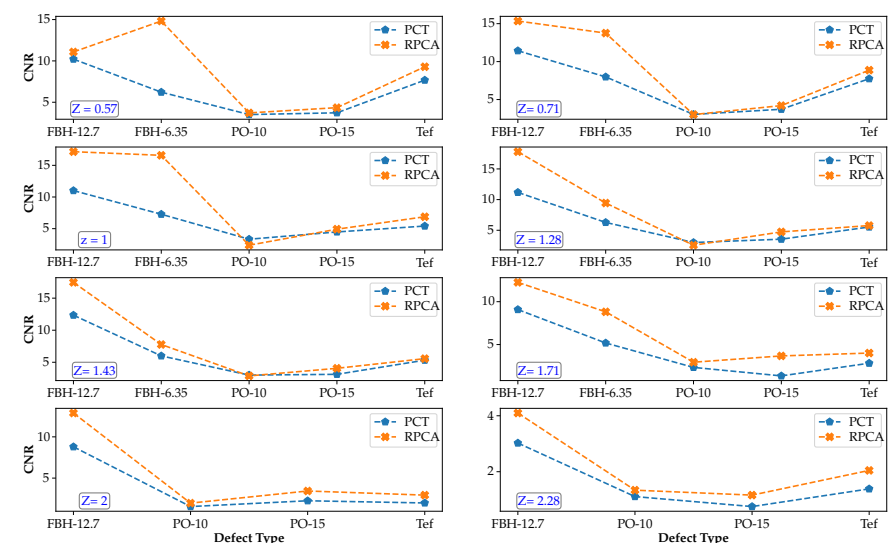


Figure 11. CNRmax by defect depth as a function of the defect type for all data sequences (PCT and RPCT).

Table 3. Maximum CNR (CNRmax) values for RPCT and PCT methods in all depths (Z).

Teflon		CNRmax			FBH D= 12.7 mm					CNRmax		PO th = 0.15 mm		CNRmax		
Code	Z	RPCT	PCT	RPCT vs. PCT	Code	Z	RPCT	PCT	RPCT vs. PCT	Code	Z	RPCT	PCT	RPCT vs. PCT		
Tef-A	2.43	1.408	1.214	16%	FBH-1J	2.28	4.098	3.025	35%	PO15-A	2.43	0.839	0.697	20%		
Tef-B	2.28	2.0465	1.3865	48%	FBH-2K	2	12.887	8.795	47%	PO15-B	2.28	1.163	0.754	54%		
Tef-B2	2.28				FBH-3L	1.71	12.255	9.081	35%	PO15-C	2.14	2.897	1.466	98%		
Tef-C	2.14	2.216	1.385	60%	FBH-4M	1.43	17.464	12.346	41%	PO15-D	2	3.439	2.254	53%		
Tef-D	2				FBH-5N	1.28	17.808	11.174	59%	PO15-E	1.86	2.399	0.908	164%		
Tef-D2	2	2.937	1.988	48%	FBH-6P	1	17.155	11.012	56%	PO15-F	1.71	3.673	1.343	173%		
Tef-E	1.86	3.085	2.457	26%	FBH-7Q	0.71	15.347	11.432	34%	PO15-G	1.57	3.994	1.906	110%		
Tef-F	1.71				FBH-8R	0.57				PO15-H	1.43	4.057	3.118	30%		
Tef-F2	1.71	4.008	2.8225	42%	FBH-8S1	0.57				PO15-J	1.28	4.734	3.545	34%		
Tef-G	1.57	4.581	3.778	21%	FBH-8S2	0.57	11.084	10.2143	9%	PO15-K	1.14	4.231	3.493	21%		
Tef-H	1.43				FBH-8S3	0.57				PO15-L	1	4.916	4.479	10%		
Tef-H2	1.43	5.5655	5.3225	5%	FBH-8S4	0.57				PO15-M	0.86	4.63	4.597	1%		
Tef-J	1.28				FBH-8S5	0.57				PO15-N	0.71	4.202	3.718	13%		
Tef-J2	1.28	5.7675	5.531	4%	FBH D= 6.35 mm					PO15-P	0.57	4.344	3.722	17%		
Tef-K	1.14	5.507	4.979	11%	CNRmax					PO15-Q	0.43	4.278	3.295	30%		
Tef-L	1				Code	Z	RPCT	PCT	RPCT vs. PCT	PO15-R	0.29	5.151	5.035	2%		
Tef-L2	1	6.8795	5.412	27%	FBH-3H	1.71	8.817	5.182	70%	PO15-S	0.14	4.65	3.595	29%		
Tef-M	0.86	9.418	6.719	40%	FBH-4G	1.43	7.769	5.993	30%	PO th=0.15 mm						
Tef-N	0.71				FBH-5G	1.28	9.44	6.277	50%	CNRmax						
Tef-N2	0.71	8.8715	7.744	15%	FBH-6F	1	16.581	7.276	128%	Code	Z	RPCT	PCT	RPCT vs. PCT		
Tef-P	0.57				FBH-7E	0.71	13.755	7.985	72%	PO10-B2	2.28	1.34	1.111	21%		
Tef-P2	0.57	9.292	7.6725	21%	FBH-8E1	0.57				PO10-D2	2	1.969	1.552	27%		
Tef-Q	0.43	6.417	7.953	−19%	FBH-8E2	0.57				PO10-F2	1.71	2.939	2.334	26%		
Tef-R	0.29	7.799	5.851	33%	FBH-8E3	0.57	14.8234	6.2194	138%	PO10-H2	1.43	2.873	2.998	−4%		
Tef-S	0.14	5.016	4.542	10%	FBH-8E4	0.57				PO10-J2	1.28	2.561	3.005	−15%		
					FBH-8E5	0.57				PO10-L2	1	2.383	3.33	−28%		
										PO10-N2	0.71	3.021	3.041	−1%		
										PO10-P2	0.57	3.711	3.51	6%		

Figure 10 shows the evolution of the CNR as a function of the depth and each processing method for each defect type. Similarly, Figure 11 shows the evolution of the CNR as a function of the material type for the raw data and each processing method for some selected defects.

Finally, Table 4 presents the best Jaccard Index score obtained for each processing method computed through time.

In the next section, the results are analyzed and discussed.

Table 4. Jaccard Index values of RPCT and PCT segmentation.

Method	RPCT	PCT
Jaccard Index	0.7395	0.7010

6. Discussion

As can be seen in Table 2, the proposed RPCT method has, for this specific and given dataset, a processing time that is considerably longer than PCT (11.5 times). This can be explained by the convex optimization operation. More precisely, to compute the low-rank and sparse matrix, several SVD are computed at each iteration of the optimization loop until it converges. Nonetheless, despite the increased time compared with the state-of-the-art methods, a computation time of 8 min 3 s is still reasonable for most NDT applications.

Approaches such as General-purpose computing on graphics processing units (GPGPU) can significantly reduce the computation time; however, such implementation exceeded this study's goals.

Several observations can be made from the results in Figures 10 and 11:

- In general, flat-bottom-holes (FBHs) present by far the highest CNR_{max} values, as expected, while pull-outs (POs) and Teflon inserts (TEFs) are very close, although with slightly higher values for the latter contrary to what was expected. Delamination-like artificial defects such as pull-outs should, in principle, present a higher thermal contrast than Teflon inserts, given that the thermo-physical properties of Teflon are closer to those of CFRP than those of air. It can be concluded that these two types of artificial defects are not different enough to produce a noticeable variation in CNR.
- In the case of FBHs at the same depth, larger defects have slightly higher CNR values than smaller defects, i.e., FBHs with $D = 12.7$ showed higher CNR_{max} than FBHs with $D = 6.35$ mm (as expected).
- For pullouts at the same depth, thicker defects have higher CNR values than thinner defects, i.e., $th = 0.15$ vs. 0.10 mm (as expected).
- Regarding the relative depths, in all cases (FBHs, POs, and TEFs), the deeper is the defect, the lower is the CNR value (as expected).
- The improvement in CNR_{max} score after processing (RPCT and PCT) is generally more pronounced for deeper depths.
- CNR values (considering all defect types) were on average 40% higher for RPCT compared to PCT, which may be taken as an indication of global performance improvement thanks to the use of RPCA.
- In the case of FBHs, CNR_{max} values were 60% higher for RPCT vs. PCT.
- In the case of POs, CNR_{max} values were 27% higher for RPCT vs. PCT.
- In the case of TEFs, CNR_{max} values were 24% higher for RPCT vs. PCT.

In the next section, we provide our conclusion regarding the proposed approach.

7. Conclusions

In this paper, we propose a new formulation of the RPCA named Orthogonal Inexact Augmented Lagrangian Multiplier (OIALM). We evaluated the performance of the resulting approach, Robust Principal Component Thermography (RPCT), for detecting defects and discontinuities in CFRP and compared the results with those of PCT using two quantitative metrics: Contrast-to-Noise Ratio (CNR) and the Jaccard similarity coefficient. The CNR

was computed frame by frame and the maximum value was identified for every defect and all techniques (raw, PCT, and RPCT).

The low-rank and sparse matrices in RPCT are projections of thermal data onto the noiseless data and noise, and the low-rank matrix is optimized in each iteration using incremental PCA. RPCT enables noise to be removed from the thermal sequences, therefore improving defect contrast and increasing defect detection.

Considering CNR results from all defect types, RPCT reported CNR_{max} values 40% higher than PCT. The improvement was greater for flat-bottom-holes (60%) compared to pull-outs (27%) and Teflon inserts (24%). In the case of the Jaccard index, RPCT performed slightly better than PCT (0.74 vs. 0.70). The computation time was however 11.5 times longer for RPCT than for PCT.

Although RPCT, to the best of our knowledge, has never been applied to pulsed thermographic data before, this study demonstrates its efficiency for defect enhancement capabilities over mixed and various types of defects typically addressed in IRT in composite materials. The goal of the study was to introduce this approach; further improvement in terms of computational speed could be achieved by using low-level programming language and hardware optimization. RPCT can therefore be considered as a powerful analysis tool that may help to push the limit of defect detection by IRT.

It should be pointed out that the RPCT method is not limited to data acquired by pulsed thermography (in which only the cooling phase is analyzed), but it could potentially be applied to other IRT techniques such as square pulse thermography (in which the heating and cooling phase may be of interest) and lockin thermography (in which regular periodic cycles are observed).

Future research will be directed towards the application of RPCT to different materials (glass fibers, aluminium, etc.), to the implementation of software/hardware optimization solutions (e.g., through the use of GPGPUs), and to the application of RPCT to other IRT techniques (e.g., square pulse thermography and lockin thermography).

Author Contributions: Conceptualization and methodology, S.E., J.F., L.-D.T., M.K., M.G., C.I.-C., and X.M.; data analysis and processing, J.F. and S.E.; experimental data acquisition, M.G., M.K., L.-D.T., and C.I.-C.; resources, L.-D.T. and X.M.; writing—original draft preparation, S.E. and J.F.; writing—review and editing, M.K., M.G., L.-D.T., C.I.-C., and X.M.; and supervision, X.M. All authors have read and agreed to the published version of the manuscript.

Funding: This research is part of the LDCOMP collaborative R&D proposal jointly funded by the Ministère de l'Économie et de l'Innovation—Québec (MEI) (File number: 2018-PI-1-SQA) and SKYWING (Wallonie, Belgium, Convention n° 8188). The authors wish to thank also the following sponsors: XIe Commission Commission mixte permanente Wallonie-Bruxelles-Québec 2019–2021 (project 11.812), NSERC CREATE «oN DuTy!» Initiative, NSERC DG program, and the Canada Research Chair in Multipolar Infrared Vision (MIVIM).

Institutional Review Board Statement: Not applicable.

Informed Consent Statement: Not applicable.

Conflicts of Interest: The funders had no role in the design of the study; in the collection, analyses, or interpretation of data; in the writing of the manuscript, or in the decision to publish the results.

Abbreviations

The following abbreviations are used in this manuscript:

ALM	Augmented Lagrangian Multiplier
APG	Accelerated Proximal Gradient
CFRP	Carbon Fiber Reinforced Plastic
CNR	Contrast to Noise Ratio
DRPCA	Double Robust Principal Component Analysis
EALM	Exact Augmented Lagrange Multiplier

ECPT	Eddy Current Pulsed Thermography
ESPCA	Edge-Group Sparse Principal Component Analysis
ESPCT	Edge-Group Sparse Principal Component Thermography
FBH	Flat Bottom Holes
GPGPU	General-purpose computing on graphics processing units
IALM	Inexact Augmented Lagrange Multiplier
ICA	Independent Component Analysis
IoU	Intersection over Union
IRT	InfraRed Thermography
LADMAP	Linearized Alternating Direction Method with Adaptive Penalty
LatLRRT	Latent Low-Rank Representation Thermography
MWIR	Mid-Wave InfraRed
NDT	Non Destructive Testing
NMF	Non-negative Matrix Factorization
NP	Non-Deterministic Polynomial
OIALM	Orthogonal Inexact Augmented Lagrange Multiplier
PCA	Principal Component Analysis
PCP	Principal Component Pursuit
PCT	Principal Component Thermography
PLS	Partial Least Square
PLST	Partial Least Square Thermography
PO	Pull-Outs
PPT	Pulsed Phase Thermography
PT	Pulsed Thermography
RPCA	Robust Principal Component Analysis
RPCT	Robust Principal Component Thermography
SNR	Signal to Noise Ratio
SPCA	Sparse Principal Component Analysis
SPCT	Sparse Principal Component Thermography
SVM	Support Vector Machine
Tef	Teflon Inserts
TSR	Thermographic Signal Reconstruction

References

- Vavilov, V.; Maldague, X. Optimization of heating protocol in thermal NDT, short and long heating pulses: A discussion. *Res. Nondestruct. Eval.* **1994**, *6*, 1–18. [\[CrossRef\]](#)
- Hotelling, H. Analysis of a complex of statistical variables into principal components. *J. Educ. Psychol.* **1933**, *24*, 417. [\[CrossRef\]](#)
- Pearson, K. LIII. On lines and planes of closest fit to systems of points in space. *Lond. Edinb. Dublin Philos. Mag. J. Sci.* **1901**, *2*, 559–572. [\[CrossRef\]](#)
- Rajic, N. Principal component thermography for flaw contrast enhancement and flaw depth characterisation in composite structures. *Compos. Struct.* **2002**, *58*, 521–528. [\[CrossRef\]](#)
- Candès, E.J.; Li, X.; Ma, Y.; Wright, J. Robust Principal Component Analysis? *J. ACM* **2011**, *58*. [\[CrossRef\]](#)
- Ebadi, S.E.; Izquierdo, E. Foreground segmentation with tree-structured sparse RPCA. *IEEE Trans. Pattern Anal. Mach. Intell.* **2017**, *40*, 2273–2280. [\[CrossRef\]](#) [\[PubMed\]](#)
- Bouwmans, T.; Zahzah, E.H. Robust PCA via principal component pursuit: A review for a comparative evaluation in video surveillance. *Comput. Vis. Image Underst.* **2014**, *122*, 22–34. [\[CrossRef\]](#)
- Luan, X.; Fang, B.; Liu, L.; Yang, W.; Qian, J. Extracting sparse error of robust PCA for face recognition in the presence of varying illumination and occlusion. *Pattern Recognit.* **2014**, *47*, 495–508. [\[CrossRef\]](#)
- Gavrilescu, M. Noise robust automatic speech recognition system by integrating robust principal component analysis (RPCA) and exemplar-based sparse representation. In Proceedings of the 2015 7th International Conference on Electronics, Computers and Artificial Intelligence (ECAI), Bucharest, Romania, 25–27 June 2015; pp. S-29–S-34.
- Deerwester, S.; Dumais, S.T.; Furnas, G.W.; Landauer, T.K.; Harshman, R. Indexing by latent semantic analysis. *J. Am. Soc. Inf. Sci.* **1990**, *41*, 391–407. [\[CrossRef\]](#)
- Song, Q.; Yan, G.; Tang, G.; Ansari, F. Robust principal component analysis and support vector machine for detection of microcracks with distributed optical fiber sensors. *Mech. Syst. Signal Process.* **2021**, *146*, 107019. [\[CrossRef\]](#)
- Yao, J.; Liu, X.; Qi, C. Foreground detection using low rank and structured sparsity. In Proceedings of the 2014 IEEE International Conference on Multimedia and Expo (ICME), Chengdu, China, 14–18 July 2014; pp. 1–6.
- Liu, X.; Zhao, G.; Yao, J.; Qi, C. Background subtraction based on low-rank and structured sparse decomposition. *IEEE Trans. Image Process.* **2015**, *24*, 2502–2514. [\[CrossRef\]](#) [\[PubMed\]](#)

14. Guyon, C.; Bouwmans, T.; Zahzah, E.H. Foreground detection based on low-rank and block-sparse matrix decomposition. In Proceedings of the 2012 19th IEEE International Conference on Image Processing, Orlando, FL, USA, 30 September–3 October 2012; pp. 1225–1228.
15. Xue, Z.; Dong, J.; Zhao, Y.; Liu, C.; Chellali, R. Low-rank and sparse matrix decomposition via the truncated nuclear norm and a sparse regularizer. *Vis. Comput.* **2019**, *35*, 1549–1566. [[CrossRef](#)]
16. Yang, B.; Zou, L. Robust foreground detection using block-based RPCA. *Optik* **2015**, *126*, 4586–4590. [[CrossRef](#)]
17. Khan, M.A.; Kim, J. Toward Developing Efficient Conv-AE-Based Intrusion Detection System Using Heterogeneous Dataset. *Electronics* **2020**, *9*, 1771. [[CrossRef](#)]
18. Zhang, S.; Zhang, Q.; Gu, J.; Su, L.; Li, K.; Pecht, M. Visual inspection of steel surface defects based on domain adaptation and adaptive convolutional neural network. *Mech. Syst. Signal Process.* **2021**, *153*, 107541. [[CrossRef](#)]
19. Fleuret, J.; Ibarra-Castanedo, C.; Lei, L.; Sfarra, S.; Usamentiaga, R.; Maldague, X. Defect detection based on monogenic signal processing. In *Algorithms, Technologies, and Applications for Multispectral and Hyperspectral Imagery XXV*; International Society for Optics and Photonics: Bellingham, WA, USA, 2019; Volume 10986, p. 109861X.
20. Yousefi, B.; Sfarra, S.; Sarasini, F.; Castanedo, C.I.; Maldague, X.P. Low-rank sparse principal component thermography (sparse-PCT): Comparative assessment on detection of subsurface defects. *Infrared Phys. Technol.* **2019**, *98*, 278–284. [[CrossRef](#)]
21. Wen, C.M.; Sfarra, S.; Gargiulo, G.; Yao, Y. Edge-Group Sparse Principal Component Thermography for Defect Detection in an Ancient Marquetry Sample. *Proceedings* **2019**, *27*, 34. [[CrossRef](#)]
22. Wen, C.M.; Sfarra, S.; Gargiulo, G.; Yao, Y. Thermographic Data Analysis for Defect Detection by Imposing Spatial Connectivity and Sparsity Constraints in Principal Component Thermography. *IEEE Trans. Ind. Inform.* **2021**, *17*, 3901–3909. [[CrossRef](#)]
23. Min, W.; Liu, J.; Zhang, S. Edge-group sparse PCA for network-guided high dimensional data analysis. *Bioinformatics* **2018**, *34*, 3479–3487. [[CrossRef](#)] [[PubMed](#)]
24. Yousefi, B.; Castanedo, C.I.; Maldague, X.P. Low-rank Convex/Sparse Thermal Matrix Approximation for Infrared-based Diagnostic System. *arXiv* **2020**, arXiv:2010.06784.
25. Yousefi, B.; Castanedo, C.I.; Maldague, X.P.V. Measuring Heterogeneous Thermal Patterns in Infrared-Based Diagnostic Systems Using Sparse Low-Rank Matrix Approximation: Comparative Study. *IEEE Trans. Instrum. Meas.* **2021**, *70*, 1–9. [[CrossRef](#)]
26. Rengifo, C.J.; Restrepo, A.D.; Nope, S.E. Method of selecting independent components for defect detection in carbon fiber-reinforced polymer sheets via pulsed thermography. *Appl. Opt.* **2018**, *57*, 9746–9754. [[CrossRef](#)] [[PubMed](#)]
27. Liu, Y.; Wu, J.Y.; Liu, K.; Wen, H.L.; Yao, Y.; Sfarra, S.; Zhao, C. Independent component thermography for non-destructive testing of defects in polymer composites. *Meas. Sci. Technol.* **2019**, *30*, 044006. [[CrossRef](#)]
28. Fleuret, J.; Ibarra-Castanedo, C.; Ebrahimi, S.; Maldague, X. Independent Component Thermography Applied to Pulsed Thermographic Data. In Proceedings of the 3rd International Symposium on Structural Health Monitoring and Nondestructive Testing, Québec City, QC, Canada, 14–15 May 2020.
29. Fleuret, J.; Ibarra-Castanedo, C.; Ebrahimi, S.; Maldague, X. Latent Low Rank Representation Applied to Thermography. In Proceedings of the 2020 International Conference on Quantitative InfraRed Thermography, Porto, Portugal, 21–30 September 2020. [[CrossRef](#)]
30. Maldague, X.; Marinetti, S. Pulse phase infrared thermography. *J. Appl. Phys.* **1996**, *79*, 2694–2698. [[CrossRef](#)]
31. Liu, K.; Li, Y.; Yang, J.; Liu, Y.; Yao, Y. Generative principal component thermography for enhanced defect detection and analysis. *IEEE Trans. Instrum. Meas.* **2020**, *69*, 8261–8269. [[CrossRef](#)]
32. Rajic, N. *Principal Component Thermography*; Technical Report; Defence Science And Technology Organisation: Victoria, Australia, 2002.
33. Liu, K.; Tang, Y.; Lou, W.; Liu, Y.; Yang, J.; Yao, Y. A thermographic data augmentation and signal separation method for defect detection. *Meas. Sci. Technol.* **2021**, *32*, 045401. [[CrossRef](#)]
34. Lopez, F.; Nicolau, V.; Maldague, X.; Ibarra-Castanedo, C. Multivariate infrared signal processing by partial least-squares thermography. In Proceedings of the 16th International Symposium on Applied Electromagnetics and Mechanics, Québec, QC, Canada, 31 July–3 August 2013.
35. Lopez, F.; Ibarra-Castanedo, C.; de Paulo Nicolau, V.; Maldague, X. Optimization of pulsed thermography inspection by partial least-squares regression. *NDT E Int.* **2014**, *66*, 128–138. [[CrossRef](#)]
36. Shepard, S.M.; Lhota, J.R.; Rubadeux, B.A.; Ahmed, T.; Wang, D. Enhancement and reconstruction of thermographic NDT data. In *Thermosense XXIV*; Maldague, X.P., Rozlosnik, A.E., Eds.; International Society for Optics and Photonics, SPIE: Bellingham, WA, USA, 2002; Volume 4710, pp. 531–535. [[CrossRef](#)]
37. Fleuret, J.; Ebrahimi, S.; Maldague, X. Pulsed Thermography Signal Reconstruction Using Linear Support Vector Regression. In Proceedings of the 2020 International Conference on Quantitative InfraRed Thermography, Porto, Portugal, 21–30 September 2020. [[CrossRef](#)]
38. Vapnik, V.N. *The Nature of Statistical Learning Theory*; Springer: New York, NY, USA, 1995.
39. Zhu, P.; Cheng, Y.; Bai, L.; Tian, L. Local sparseness and image fusion for defect inspection in eddy current pulsed thermography. *IEEE Sens. J.* **2018**, *19*, 1471–1477. [[CrossRef](#)]
40. Zhu, P.P.; Cheng, Y.H.; Bai, L.B. A Novel Feature Extraction Approach for Defect Inspection in Eddy Current Pulsed Thermography. *J. Electron. Sci. Technol.* **2020**, *18*, 1–10. [[CrossRef](#)]

41. Liang, Y.; Bai, L.; Shao, J.; Cheng, Y. Application of Tensor Decomposition Methods In Eddy Current Pulsed Thermography Sequences Processing. In Proceedings of the 2020 International Conference on Sensing, Measurement & Data Analytics in the Era of Artificial Intelligence (ICSMD), Xi'an, China, 15–17 October 2020; pp. 401–406.
42. Lu, C.; Feng, J.; Chen, Y.; Liu, W.; Lin, Z.; Yan, S. Tensor robust principal component analysis with a new tensor nuclear norm. *IEEE Trans. Pattern Anal. Mach. Intell.* **2019**, *42*, 925–938. [[CrossRef](#)]
43. Xiao, X.; Gao, B.; Woo, W.L.; Tian, G.Y.; Xiao, X.T. Spatial-time-state fusion algorithm for defect detection through eddy current pulsed thermography. *Infrared Phys. Technol.* **2018**, *90*, 133–145. [[CrossRef](#)]
44. Peng, C.; Chen, Y.; Kang, Z.; Chen, C.; Cheng, Q. Robust principal component analysis: A factorization-based approach with linear complexity. *Inf. Sci.* **2020**, *513*, 581–599. [[CrossRef](#)]
45. Sun, W.; Du, Q. Graph-regularized fast and robust principal component analysis for hyperspectral band selection. *IEEE Trans. Geosci. Remote Sens.* **2018**, *56*, 3185–3195. [[CrossRef](#)]
46. Liu, Y.; Gao, X.; Gao, Q.; Shao, L.; Han, J. Adaptive robust principal component analysis. *Neural Netw.* **2019**, *119*, 85–92. [[CrossRef](#)] [[PubMed](#)]
47. Wang, Q.; Gao, Q.; Sun, G.; Ding, C. Double robust principal component analysis. *Neurocomputing* **2020**, *391*, 119–128. [[CrossRef](#)]
48. Ma, S.; Aybat, N.S. Efficient optimization algorithms for robust principal component analysis and its variants. *Proc. IEEE* **2018**, *106*, 1411–1426. [[CrossRef](#)]
49. Van Luong, H.; Deligiannis, N.; Seiler, J.; Forchhammer, S.; Kaup, A. Compressive Online Robust Principal Component Analysis via $n - \ell_1$ Minimization. *IEEE Trans. Image Process.* **2018**, *27*, 4314–4329. [[CrossRef](#)] [[PubMed](#)]
50. Cai, H.; Hamm, K.; Huang, L.; Li, J.; Wang, T. Rapid Robust Principal Component Analysis: CUR Accelerated Inexact Low Rank Estimation. *IEEE Signal Process. Lett.* **2021**, *28*, 116–120. [[CrossRef](#)]
51. Lin, Z.; Chen, M.; Ma, Y. The augmented lagrange multiplier method for exact recovery of corrupted low-rank matrices. *arXiv* **2010**, arXiv:1009.5055.
52. Candès, E.J.; Recht, B. Exact matrix completion via convex optimization. *Found. Comput. Math.* **2009**, *9*, 717–772. [[CrossRef](#)]
53. Ross, D.A.; Lim, J.; Lin, R.S.; Yang, M.H. Incremental learning for robust visual tracking. *Int. J. Comput. Vis.* **2008**, *77*, 125–141. [[CrossRef](#)]
54. Beaumont, P.W.; Zweben, C.H.; Gdutos, E.; Talreja, R.; Poursartip, A.; Clyne, T.W.; Ruggles-Wrenn, M.B.; Peijs, T.; Thostenson, E.T.; Crane, R.; et al. *Comprehensive Composite Materials II*; Elsevier: Amsterdam, The Netherlands, 2018.
55. Blain, P.; Vandenrijt, J.F.; Languy, F.; Kirkove, M.; Thérout, L.D.; Lewandowski, J.; Georges, M. Artificial defects in CFRP composite structure for thermography and shearography nondestructive inspection. In Proceedings of the Fifth International Conference on Optical and Photonics Engineering, Singapore, 4–7 April 2017; International Society for Optics and Photonics: Bellingham, WA, USA, 2017; Volume 10449, p. 104493H.
56. Vandenrijt, J.F.; Lièvre, N.; Georges, M.P. Improvement of defect detection in shearography by using principal component analysis. In *Interferometry XVII: Techniques and Analysis*; International Society for Optics and Photonics: Bellingham, WA, USA, 2014; Volume 9203, p. 92030L.
57. Kirkove, M.; Zhao, Y.; Blain, P.; Vandenrijt, J.F.; Georges, M. Thermography-inspired processing strategy applied on shearography towards nondestructive inspection of composites. In *Optical Measurement Systems for Industrial Inspection XI*; International Society for Optics and Photonics: Bellingham, WA, USA, 2019; Volume 11056, p. 110560G.
58. Usamentiaga, R.; Ibarra-Castanedo, C.; Maldague, X. More than fifty shades of grey: Quantitative characterization of defects and interpretation using SNR and CNR. *J. Nondestruct. Eval.* **2018**, *37*, 1–17. [[CrossRef](#)]
59. Jaccard, P. Lois de distribution florale dans la zone alpine. *Bull. Société Vaudoise Sci. Nat.* **1902**, *38*, 69–130. [[CrossRef](#)]
60. Tomasi, C.; Manduchi, R. Bilateral filtering for gray and color images. In Proceedings of the Sixth International Conference on Computer Vision (IEEE Cat. No. 98CH36271), Bombay, India, 7 January 1998; pp. 839–846.